Article

Effects of Zn and H Association with Naphthalene Diimide Electrodes for Aqueous Zn-ion Batteries

Moony Na, Yusik Oh, and Hye Ryung Byon

Chem. Mater., **Just Accepted Manuscript** • DOI: 10.1021/acs.chemmater.0c02357 • Publication Date (Web): 13 Jul 2020

Effects of Zn^{2+} and H^+ Association with Naphthalene Diimide Electrodes for Aqueous Zn-ion Batteries

Moony Na[1,2], Yusik Oh,[1,2] and Hye Ryung Byon[1,2,*]

[1]Department of Chemistry, Korea Advanced Institute of Science and Technology (KAIST), 291 Daehak-ro, Yuseong-gu, Daejeon 34141, Republic of Korea

[2]Advanced Battery Center, KAIST Institute for NanoCentury, 291 Daehak-ro, Yuseong-gu, Daejeon 34141, Republic of Korea

ABSTRACT: Organic electrodes have been extensively developed to enhance cycling performance in aqueous zinc (Zn)-ion cells. However, little is known about an ion-association process, which caused insufficient diagnoses of various cyclability results. Protons (H^+) are charge carriers alongside Zn^{2+} ions in mildly acidic electrolyte solutions and preferentially participate in the storage process. In addition, dissociation of water can supply the additional H^+, and the increased pH yields the precipitate of zinc hydroxy sulfate. Here, we demonstrated the critical effect of the H^+ for cycling stability of Zn-ion cells, using a 1,4,5,8-naphthalene diimide (NDI) electrode. Stepwise electron transfer of the NDI electrode proceeded via surface association of the charge carriers and subsequent solid-state diffusion. The H^+ intercalation to the NDI electrode became pronounced with an increasing current rate and led to the dissolution of the NDI molecules. We exhibited stable 1000 cycles with a capacity retention of 93.8% by suppression of the H^+ impact, and suggested a solution-mediated NDI re-assembly mechanism as the core reason for the capacity fading.

Introduction

Aqueous batteries have regained the spotlight due to the increasing desire for low-cost batteries that provide safe energy storage.[1, 2] Much attention has been directed to the multivalent ion-based system to compensate for low energy density, which arises from the narrow potential window of water.[3] Zn-ion batteries have been extensively investigated, because a Zn foil can be directly employed as a negative electrode.[4-6] However, the electrochemistry of the positive electrode does not involve the desired Zn^{2+} ion only. Protons (H^+) are charge carriers alongside Zn^{2+} ions in mildly acidic solutions.[7, 8] H^+ has unrivaled ionic mobility via a unique proton hopping process that occurs in aqueous media, called the *Grotthuss* mechanism, and they often occupy the active sites in the electrode.[7, 9] This H^+ engagement significantly influences cell performance. Several intercalation and conversion electrodes, such as those in the MnO_2, V_2O_5, and $V_2(PO_4)_3$ families, showed the co-insertion of H^+, Zn^{2+}, and water, which caused chemical conversion, volume expansion, and phase transformation.[10] Compared to those of metal oxide, organic electrodes are more flexible in accommodating these charge carriers,[11] and afford prolonged cyclability.[12, 13] However, little is still known about the Zn^{2+} and H^+ uptake in the organic electrodes, and the effect of their association for cell performance. Organic electrodes containing carbonyl groups, such as *p*-chloranil, calix[4]quinone, pyrene-4,5,9,10-tetraone, and phenanthrenequinone, exhibited Zn^{2+} coordination.[13, 14] However, evidence for Zn^{2+} association from elemental analyses should be considered carefully, because the zinc hydroxy sulfate, which often precipitates out during H^+ uptake, overlaps the Zn–O signal.[15, 16] The possible H^+ association to the reduced carbonyl group has been rarely investigated despite the well-known H^+ transfer reactions for carbonyl groups such as quinone/hydroquinone redox couple.[17] In contrast, polyaniline (PANI) and phenazine electrodes recently showed the predominant H^+ uptake, indicating the strong interaction between the amine group and H^+.[18-20] The preferential ion association may rely on surface functionalities of organic electrodes, electrolyte concentrations, and applied current rates. However, the effect of H^+ association correlated with the aqueous cell performance has not been studied yet.

Here, we investigated the Zn^{2+} and H^+ storing process using an 1,4,5,8-naphthalene diimide (NDI) electrode and demonstrated the significant impact of H^+ association on cycling stability. The NDI formed the anion radical, followed by the dianion through two-electron ($2e^-$) transfer processes. We revealed the stepwise electron transfer in a 1 M Zn^{2+} aqueous solution, where the H^+ uptake by the NDI particle became significant with an increasing current rate. In particular, the H^+ diffusion inside the NDI particle triggered the solvation of NDI, which resulted in the loss of NDI molecules. The stable 1000 cycles for the Zn–NDI cells were only achieved by suppressing the H^+ intercalation.

This report discloses the critical features of the organic electrode to alleviate H^+ intercalation.

Results and Discussions

Electrochemical analyses of an NDI electrode containing Zn^{2+} and H^+ ions. NDI is an excellent electron-acceptor and *n*-type organic semiconductor.[21] The imide group is tolerant of hydrolysis, while the carbonyl groups participate in a sequential electrochemical reduction reaction (**Figure 1a**). In addition, NDI has strong intermolecular interactions via short-range π–π stacking and hydrogen bonding, which are responsible for its solvation resistance in aqueous electrolyte solutions.[22] As-synthesized NDI particles had a triclinic crystal structure with a submicron size polyhedron shape (**Figures S1–2**) and were insoluble in the aqueous electrolyte solution. These NDI particles (60 wt%) were mixed with Super P carbon (30 wt%) and PVdF binder (10 wt%) to prepare NDI electrodes on the porous carbon paper.

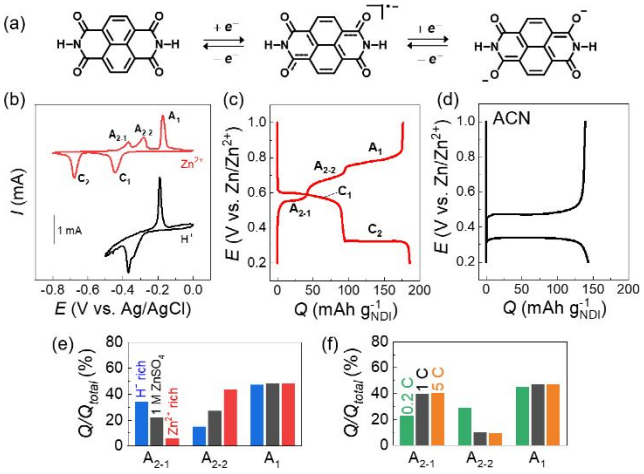

Figure 1. Electrochemical analysis of NDI electrodes in aqueous electrolyte solutions. (a) Schematic illustration of two-electron transfer for NDI molecule. (b) Cyclic voltammograms (CVs) of NDI electrodes with 1 M of $Zn(OTf)_2$ (top) and 1 M HOTf (bottom) aqueous solutions. The scan rates were 0.2 mV s^{-1}. $\mathbf{C_1}$ ($\mathbf{A_1}$) and $\mathbf{C_2}$ ($\mathbf{A_2}$) indicate the first and second cathodic (anodic) reactions, respectively. (c-d) Galvanostatic profiles of Zn–NDI cell at 0.2 C with (c) 1 M $ZnSO_4$ in water, (d) 1 M $Zn(OTf)_2$ in acetonitrile (ACN). (e–f) Comparisons of charging capacity ratios with (e) different electrolyte solutions, 1 M $ZnSO_4$ + H_2SO_4(aq) at a pH of 2.3 (blue), 1 M $ZnSO_4$(aq) (black), and 3 M $ZnSO_4$(aq) (red), and with (f) different current rates, 0.2 C (green), 1 C (black), and 5 C (orange).

A Zn^{2+} aqueous solution with 1–3 M of electrolyte salt typically has a pH of 4–5 because the multivalent ion acts as a weak acid through acid hydrolysis, according to **Eq. 1**,[23]

$$\boldsymbol{M}(H_2O)_x^{n+} \rightleftarrows \boldsymbol{M}(H_2O)_{x-1}(OH)^{(n-1)+} + H^+ \qquad \text{[Eq. 1]}$$

where $\mathbf{M^{n+}}$ is the metal ion, *n* is the multivalent state, and *x* is the number of hydrated water molecules. The Zn^{2+} is coordinated to the weakly dissociating base, while the separated H^+ ion (10^{-4}–10^{-5} M with a pH of 4–5) causes the mildly acidic conditions. Therefore, we consider two positive charge carriers, Zn^{2+} and H^+, for the charge storing process. These charge carriers' valence states, hydrations, and diffusivities significantly dictate the electron transfer process of the NDI electrode.[24, 25] The electrochemical behaviors of the NDI electrodes were firstly examined by cyclic voltammetry (CV) using three-electrode cells. The NDI with 1 M of $Zn(OTf)_2$(aq) typically showed stepwise cathodic waves at –0.44 V ($\mathbf{C_1}$) and –0.68 V ($\mathbf{C_2}$) vs. Ag/AgCl (**Figure 1b**). The corresponding anodic responses were split into three waves, –0.37 V ($\mathbf{A_{2\text{-}1}}$), –0.28 V ($\mathbf{A_{2\text{-}2}}$), and –0.17 ($\mathbf{A_1}$). The two smaller peaks belonged to $\mathbf{A_2}$, the response to $\mathbf{C_2}$, while the intense anodic signal was assigned to $\mathbf{A_1}$ (**Figure S3**). In addition, we could measure the numbers of electron transfer from the capacity of the aqueous Zn–NDI cells, where the NDI electrode was assembled from metallic Zn foil and 1 M $ZnSO_4$(aq) electrolyte solution (**Figure 1c**). The galvanostatic profile of aqueous Zn–NDI cells is consistent with the CV results.[13, 26] The $\mathbf{C_2}$ capacity was almost equivalent to that of the $\mathbf{C_1}$, and the total capacity ($\mathbf{C_1}$ + $\mathbf{C_2}$) at ~185 mAh g^{-1}_{NDI} was ~92% of the theoretical value (201 mAh g^{-1}_{NDI}). This behavior verified a stepwise 1e$^-$ transfer of the NDI at the $\mathbf{C_1}$ and $\mathbf{C_2}$ regions.

To identify the $\mathbf{C_1}$ reaction, we switched the electrolyte solution to 1 M of HOTf(aq), where H^+ is the sole positive charge carrier. The CV curve showed two cathodic waves successively at –0.34 and –0.37 V, around the $\mathbf{C_1}$ potential region (Figure 1b). The H^+ provided the most positive potentials among other monovalent ions, such as K^+ (–0.40, –0.43 V, **Figure S4**) and Li^+ (–0.50, –0.54 V) due to its fast mobility in the aqueous solution, while the hydrogen evolution reaction occurred below –0.5 V due to the strongly acidic condition. The single $\mathbf{C_1}$ wave from the Zn^{2+} aqueous solution had 70 mV more negative than that from H^+. Furthermore, the $\mathbf{C_1}$ potential from Zn^{2+} fell between those of the K^+ and Li^+ solutions, which was in line with the Zn^{2+} mobility in an infinitely dilute solution (**Table S1**). This comparison seemingly indicates the predominant Zn^{2+} association with the radical anion of NDI^- during the $\mathbf{C_1}$.

A similar $\mathbf{C_2}$ wave was observed from a non-aqueous (water-free) Zn^{2+} electrolyte solution. The $\mathbf{C_2}$ plateau at ~0.3 V (vs. Zn/Zn^{2+}, unless otherwise noted) was distinguishable from the $\mathbf{C_1}$ potential at ~0.6 V, whereas it overlapped with the single potential plateaus from the non-aqueous Zn–NDI cells (1 M $Zn(OTf)_2$/acetonitrile (ACN), **Figures 1c–d** and **S5–6**). However, corresponding charging processes for $\mathbf{A_2}$ were entirely different from the two cells. The $\mathbf{A_{2\text{-}1}}$ (0.55 V) and $\mathbf{A_{2\text{-}2}}$ (0.7 V) plateaus emerged in the aqueous Zn–NDI cells, whereas the single $\mathbf{A_2}$ plateau (0.47 V) appeared in the ACN electrolyte solution. Furthermore, the charging capacities of $\mathbf{A_{2\text{-}1}}$ and $\mathbf{A_{2\text{-}2}}$ were governed by the Zn^{2+} and H^+ concentrations in the aqueous electrolyte solutions. In the standard 1 M $ZnSO_4$(aq) solution (pH = 5.2), the capacity ratios of $\mathbf{A_{2\text{-}1}}$ and $\mathbf{A_{2\text{-}2}}$ were 23 and 28%, respectively, at 0.2 C (**Figures 1e–f**). The total capacity of $\mathbf{A_2}$ (i.e., $\mathbf{A_{2\text{-}1}}$ + $\mathbf{A_{2\text{-}2}}$) was comparable to that of $\mathbf{A_1}$ (49%). When increasing the H^+ concentration, by adjusting the pH to 2.8, the $\mathbf{A_{2\text{-}1}}$ capacity ratio increased to 35% while that of $\mathbf{A_{2\text{-}2}}$ shrank by 16% (**Figures 1e** and **S7a**). In contrast, the 3 M $ZnSO_4$(aq) solution (pH = 4.3) increased the $\mathbf{A_{2\text{-}2}}$ capacity to

45% and reduced that of $\mathbf{A_{2\text{-}1}}$ to 7%. Consequently, the $\mathbf{A_{2\text{-}1}}$ and $\mathbf{A_{2\text{-}2}}$ correspond to the H^+ and Zn^{2+} concentrations, respectively. In addition, the $\mathbf{A_2}$ capacity is influenced by the current rates. When increasing the rate from 0.2 to 1 C, the $\mathbf{A_{2\text{-}1}}$ capacity also increased; namely, the H^+ uptake is dominant for the $\mathbf{C_2}$ at rates of 1 C (**Figures 1f** and **S7b**).[20] On the contrary, the Zn^{2+} insertion was prominent at lower current rates, as supported by the negligible $\mathbf{A_{2\text{-}1}}$ in the CV curve at 0.05 mV s^{-1} (**Figure S8**). These results demonstrate that two positive charge carriers participated in the ion association during the $\mathbf{C_2}$, and the test conditions determined the preferential charge carrier.

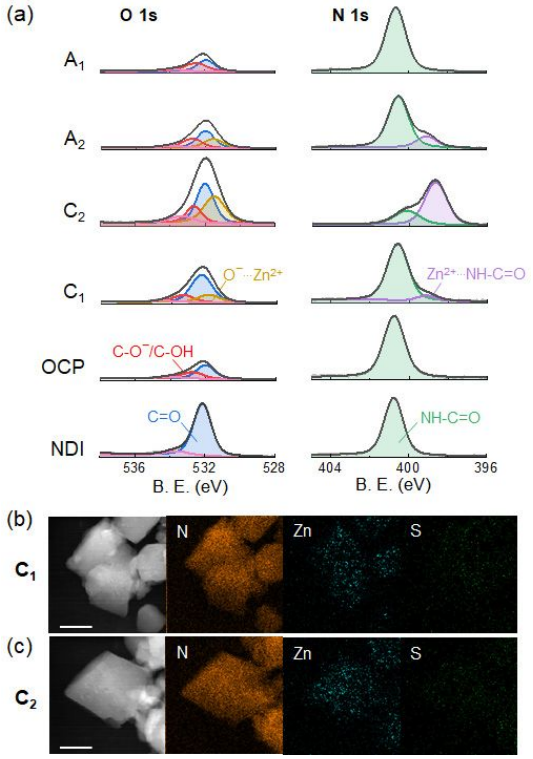

Figure 2. Evidence of Zn^{2+} uptake and extraction by using XPS and elemental mapping images. The NDI electrodes were examined with 1 M $ZnSO_4$(aq) at 0.2 C and dried in a vacuum. (a) XPS analysis of NDI electrodes in O 1s (left) and N 1s (right) binding energy (BE) regions at different discharging and charging stages. The OCP indicates an open-circuit potential state. (b–d) STEM-EDS mapping images of NDI particles (b) after $\mathbf{C_1}$, and (c) after $\mathbf{C_2}$. Orange, blue, and green dots are nitrogen, zinc, and sulfur element, respectively. The scale bars are 100 nm.

Chemical evidence for Zn^{2+} and H^+ uptake in aqueous Zn-NDI cells. We investigated the Zn^{2+} and H^+ uptake of discharged and charged NDI electrodes using various chemical analyses. The Zn^{2+} uptake was studied by X-ray photoelectron spectroscopy (XPS). As-synthesized NDI (**Figure 2a**) showed the C=O signal (532.0 eV in the O 1s binding energy (BE) region) and N–C=O from the imide group (400.8 eV in the N 1s BE region).[27] The marginal signal in O 1s spectrum (light pink, 533.8 eV, <5 at.% quantity) is assigned to the carboxyl group, arising from the hydrolyzed precursor, 1,4,5,8-naphthalene tetracarboxylic dianhydride (NTCDA). The NDI electrode containing Super P carbon and PVdF binder displayed the additional C–OH (532.8 eV) and CF_2 moieties (291.4 eV, **Figure S9**), analyzed after resting at open circuit potential (OCP).[28, 29] When the $\mathbf{C_1}$ terminated at 0.2 C, the Zn–O signal emerged at 531.4 eV. Moreover, a new shoulder appeared in the N 1s region at a lower BE (399.3 eV) by the Zn^{2+} coordination to the amine group (Zn^{2+}…NHC=O).[30, 31] This Zn^{2+} coordination peak was pronounced after the $\mathbf{C_2}$, demonstrating the Zn^{2+} uptake. For the charging process, these coordination signals were attenuated and eliminated at the end of $\mathbf{A_1}$. The Zn^{2+} uptake was also supported by elemental mapping images of NDI particles. A scanning transmission electron microscopy (STEM)–linked energy dispersive X-ray spectrometer (EDS) mapped the uniform distribution of Zn in the polyhedral NDI particles after $\mathbf{C_1}$ and $\mathbf{C_2}$ (**Figures 2b–c**). In contrast, S, from the sulfate (SO_4^{2-}) ions, was not visible in the NDI particles. We note that these NDI particles were separated from byproducts, zinc hydroxy sulfate, having flake or granular shape (see below).

Further, the H^+ association with the NDI could be verified by the zinc hydroxy sulfate byproducts. The $ZnSO_4[Zn(OH)_2]_3{\cdot}nH_2O$ is yielded at high local pH of the electrolyte solution, where the zinc hydroxide coordinates to SO_4^{2-} and settles into the electrode.[32] This local pH rise can be created by the loss of H^+ from the electrolyte solution. The amine/imide-containing organic electrodes and MnO_2 cells showed the predominant H^+ uptake in precipitating the zinc hydroxy sulfate,[8, 18-20] which made the pH of the entire solution constant.[18] In our system, the air-drying NDI electrodes had an intense 001 reflection of $ZnSO_4[Zn(OH)_2]_3{\cdot}4H_2O$ at 2θ = 8.55º from X-ray diffraction (XRD, **Figure S10**). In addition, the pentahydrate of $ZnSO_4[Zn(OH)_2]_3$ appeared after the 2nd discharge (**Figure S11**). Attenuated total reflectance-infrared (ATR-IR) spectra also exhibited the symmetric stretching vibrations of the SO_4^{2-} group at 1114.3 and 1157 cm^{-1} after $\mathbf{C_1}$, which became very pronounced after $\mathbf{C_2}$ (**Figures 3a** and **S12**).[32] At the end of $\mathbf{C_2}$, the electrode surface turned white, and micron flake-shaped precipitates covered the surface (**Figures 3b–d**). The numerous precipitates implicate that the resource of H^+ is not limited by the mildly acidic solution that contains only ~10^{-5} M of H^+, but is supplied by dissociation of water.[8] The dissociation of water, forming H^+ and OH^- under the applied electric field, was observed in the vicinity of the charged surface group from ion-exchange membranes.[33-35] Besides, the hydration shell of the divalent Zn^{2+} containing the weakly dissociating base (Eq. 1) can promote the dissociation of water further.[35, 36] Thus, it is suggested that the negatively charged NDIs intimately interact with water molecules, followed by H^+ transfer before the Zn^{2+} uptake. This process is supposed to be different from the H^+ electrochemistry showing the CV profile with 1 M HOTf(aq) (Figure 1b). During the charging process, the H^+ was extracted, and the zinc hydroxy sulfate was dissolved. The SO_4^{2-} modes were attenuated in the ATR-IR spectra after $\mathbf{A_2}$ and vanished at the end of $\mathbf{A_1}$. In addition, the color of the electrode surface returned to black. However, the XRD pattern of $ZnSO_4[Zn(OH)_2]_3{\cdot}4H_2O$ was still intense after $\mathbf{A_2}$. Furthermore, the remaining XRD signal after $\mathbf{A_1}$ reflected incomplete H^+ extraction (Figure S10). The XPS signals of $ZnSO_4[Zn(OH)_2]_3{\cdot}4H_2O$ may overlay

those of Zn^{2+} and OH. The increased Zn–O signal is also related to the substantial formation of the zinc hydroxy sulfate (Figure 2a), which is supported by the increase in the O atomic % during discharge (**Figure S13**). This byproduct could not be completely removed even after washing and drying processes.

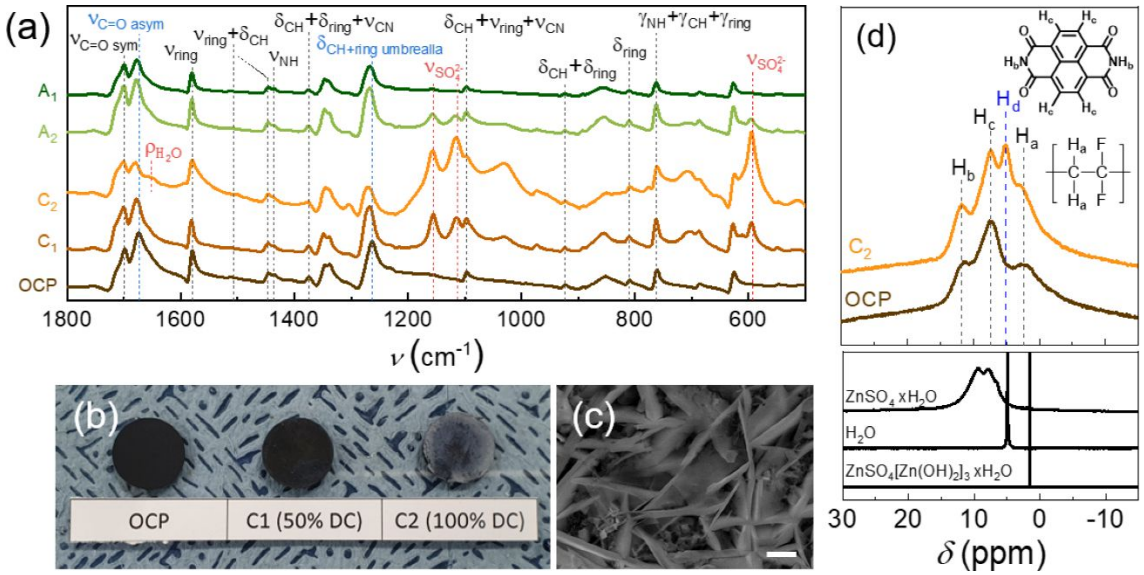

Figure 3. Characterizations of $ZnSO_4[Zn(OH)_2]_3{\cdot}4H_2O$ byproduct. The NDI electrodes were examined with 1 M $ZnSO_4$(aq) at 0.2 C and dried in air. (a) ATR-IR spectra of NDI electrodes with different discharging and charging stages. (b) Digital photo of NDI electrodes at OCP (as prepared), after $\mathbf{C_1}$, and after $\mathbf{C_2}$. (c) SEM image of NDI electrodes after $\mathbf{C_2}$. The scale bars indicate 2 μm. (d) Solid-state (ss) ^{1}H NMR spectra of NDI electrodes at OCP (black) and after the $\mathbf{C_2}$ (orange). The inset indicates each moiety labeled to H_a~H_c. The bottom panel shows ss ^{1}H NMR of the standard references.

Noteworthy is that the electrochemical reduction of the NDI was not explicitly exhibited by the IR vibration spectroscopy. Typically, the carbonyl group of the NDI weakens its stretching band, while the enolate band appeared and became enhanced during the discharge. Previous studies showed the increasing enolate signals by adding the Li^+, K^+, or Mg^{2+} ions.[37-39] However, the NDI electrodes in the Zn cells only showed the attenuated $\nu_{C=O,anti-sym}$ band without the enolate signal after the $\mathbf{C_2}$ (Figure S12). A similar characteristic was reported for a 3,4,9,10-perylenetetracarboxylic dianhydride (PTCDA) electrode and was ascribed to the screening of H^+ by the water cluster.[37] Indeed, we also observed the water cluster inside the NDI electrodes by using solid-state ^{1}H NMR spectroscopy. The as-prepared NDI electrode that was rested at OCP had three resonances, the methylene group of the PVdF binder (H_a, 2.4 ppm), the aromatic ring (H_c, 7.3 ppm) of the NDI, and the N–H group (H_b, at 11.8 ppm) (**Figure 3d**).[40, 41] After the $\mathbf{C_2}$, a new signal emerged at 5.1 ppm, which was assigned to the water cluster inside the NDI. This ^{1}H resonance was distinct from the water signals from $ZnSO_4[Zn(OH)_2]_3{\cdot}4H_2O$ (1.5 ppm), and the hydrated $ZnSO_4$ ($ZnSO_4{\cdot}xH_2O$, 6.5–9.5 ppm). In comparison with the bulk water peak (4.95 ppm),[16] the discharged NDI electrode had the proton downfield and a broader shape. This characteristic was typically observed from the confined water cluster.[42] The insertion of the water cluster into the NDI particle might be attained by the H^+ uptake and their hydrogen bonding.

The proposed, solution-mediated re-assembly mechanism. The evolution of the NDI structure and size reveals the effect of ion association. During the $\mathbf{C_1}$, the NDI structure was marginally changed. The XRD reflections of the triclinic NDI structure slightly broadened (**Figure 4a**), and scanning electron microscopy (SEM) images displayed a negligible deformation of the NDI shape and size (**Figures 4b–c**). These characteristics are attributed to the surface reaction of the NDI.[43] The surface association and dissociation processes of the positive charge carriers are fast without the perturbation of electrode structure, and minimally dependent on the test conditions (**Figures 1e–f**).

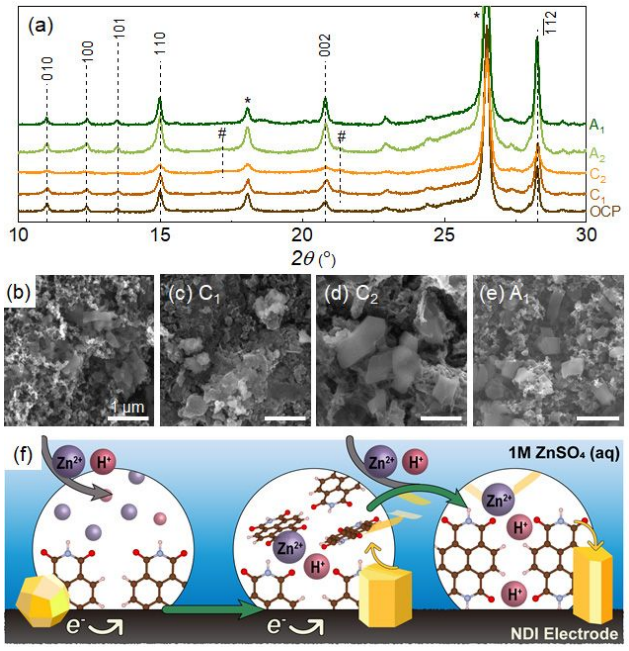

Figure 4. Characterizations of NDI particle structures. The NDI electrodes were examined with 1 M $ZnSO_4$(aq) at 0.2 C and dried in air for (a, f) or vacuum for (b–e) samples. (a) XRD patterns of NDI electrodes. The facets of triclinic NDI crystal are indicated. The asterisk (*) and hash (#) symbols denote the reflections of porous carbon substrate and $ZnSO_4[Zn(OH)_2]_3{\cdot}4H_2O$, respectively. (b–e) SEM images of NDI electrodes (b) as-prepared, (c) after C_1, (d) after C_2, and (e) after A_1. The scale bars indicate 1 μm. (f) Schematic illustration for solution-mediated assembly of NDI during the discharging process.

By comparison, the $\mathbf{C_2}$ has a large polarization in the galvanostatic profile (**Figure 1c**). It is attributed to the intercalation and solid-state diffusion of hydrated H^+ and Zn^{2+} inside of the NDI particles. The single reduction wave at $\mathbf{C_2}$ suggests the negligible energy difference for H^+ and Zn^{2+} intercalation, although the prominent ions are determined from the current rate (or scan rate). In addition, this bulk process accompanies the dissolution of the NDI molecules. The H^+ and water extend the interlayered and intermolecular distance between the NDI molecules. The loose π–π interaction for stacking direction and the weaken hydrogen bonding for the in-plain direction of NDI molecules promote the facile solvation of dianionic NDI (NDI^{2-}) molecules. Then, the solvated NDI molecules containing hydrated H^+ or Zn^{2+} are assembled and re-precipitated through π–π interaction, indicated as the solution-mediated assembly process. As a result, the NDI particles become enlarged, revealing ~1 μm of size (**Figure 4d**). The XRD pattern showed the broad crystalline reflections of the NDI particles at the end of $\mathbf{C_2}$. The intensities were significantly attenuated (**Table S2**), reflecting the formation of mostly amorphous NDI particles after $\mathbf{C_2}$. This solution-mediated assembly process is depicted in **Figure 4f**.

During the charging process, two potential regions of $\mathbf{A_{2\text{-}1}}$ and $\mathbf{A_{2\text{-}2}}$ emerge during the $\mathbf{A_2}$ process. It is caused by the extraction of the Zn^{2+} and the H^+ with different solid-state diffusions. The extraction of hydrated H^+ and Zn^{2+} from *inside* of the NDI particle moderately reduces the particular size at $\mathbf{A_2}$ (**Figure S14**). However, the subsequent surface reaction for $\mathbf{A_1}$, i.e., the extraction of H^+ and Zn^{2+} from the *surface* of the NDI, does not visibly change the particular size (**Figure 4e**). The crystalline reflections became intense during the charging process (**Figures 4a** and **Table S2**). In comparison with the as-prepared NDI electrodes, the 110, 002, and $\bar{1}\bar{1}2$ become pronounced after the $\mathbf{A_2}$ and $\mathbf{A_1}$ (Figure 4a). We anticipate that this structural transition was mostly established during the $\mathbf{C_2}$ through the solution-mediated assembly process, while the intercalated charge carriers made the featureless pattern. After the bulk extraction process at the $\mathbf{A_2}$, the crystalline pattern appears. Overall, there is a negligible solution-meditated process during $\mathbf{A_2}$~$\mathbf{A_1}$.

Cell performances relied on the solution-mediated process. The challenge of this solution-mediated re-assembly process is the possible loss of NDI molecules due to dissolution, which leads to swift capacity fading for a cycling test.[37] It is akin to the inferior cyclability of the non-aqueous Zn–NDI cells, where the intimate interaction between the NDI molecules and the ACN solvent sharply reduced the cycling capacity (**Figure S15**). Similarly, the capacity faded by half (~100 mAh g^{-1}_{NDI}) for 50 cycles at 1 C in the aqueous medium (**Figures 5a** and **S16**). At 1 C, the H^+ intercalation into the NDI particle is superior to that of the Zn^{2+} ion (Figure 1f); thereby, the solvation of NDI^{2-} molecules was expedited. The increasing current rate exacerbated the cycling stability (**Figure 5b**), and the IR vibrations of the NDI molecules were observed from the separator (**Figure S17**). The Zn–NDI cells with 3 M $ZnSO_4$(aq) also showed no improvements in the cycling stability at 1 C rate, exhibiting >65% capacity fading for 50 cycles (**Figure S18**).

A viable method to ameliorate the cycling performance is preventing the H^+ and water intercalation into the NDI electrode during the $\mathbf{C_2}$. The cutoff potential by the $\mathbf{C_1}$ reaction rendered a marginal change of NDI particle size caused by the surface association of charge carriers. Moreover, the byproduct was moderately formed on the electrode surface, as revealed by the black color of the electrode surface (Figure 3b). We demonstrated that the discharging stage, limited by $\mathbf{C_1}$ (0.4–1.0 V), was stable for 1000 cycles at 1 C (**Figure 5e**). The total capacity retention and Coulombic efficiency (CE) were estimated to be 93.8% and 99.1%, respectively. In addition, the voltage polarization and capacity drop were moderate as the current rate increased, which was the crucial advantage of the surface reaction (**Figure S19**). The rate capability was excellent at 2 C, and the original capacity level at 1 C was regained, even after testing at 10 C. (**Figure 5d**). At 2 C, the Zn–NDI cells also successfully performed over 600 cycles (**Figure S20**). In addition, after 100 cycles at 5 C, the NDI vibrations were not detected from the separator (Figure S17), verifying the insignificant NDI solvation in the $\mathbf{C_1}$–$\mathbf{A_1}$ region. The surface implementation of Zn^{2+} and H^+ is fast and does not deteriorate the NDI particles. The improved cycling performance of Zn–NDI cells demonstrated that the key processes of NDI electrochemical reactions are the mitigation of the H^+ intercalation to the inside of the NDI particle. On the other hand, this mechanistic study suggests the direction of future research for molecular design. Increasing intermolecular interaction is needed to suppress the molecular solubility during the electrochemical reactions. This approach will enhance the capacity and stability of long-term cyclability.

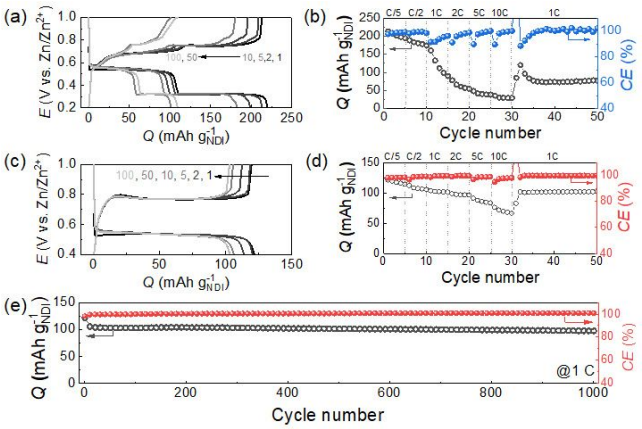

Figure 5. Comparative cycling performances of Zn–NDI cells with 1 M $ZnSO_4$(aq) with different discharging depths. (a, c) Galvanostatic profiles in a potential range of (a) 0.2–1.0 V and (c) 0.4–1.0 V, under the condition at 1 C. (b, d) Corresponding rate-capability results from 0.2 C to 10 C. (e) Prolonged cycling stability and Coulombic efficiency (CE) in a potential range of 0.4–1.0 V. The current rate was 1 C.

Conclusion

We demonstrated the ion-association process of the positive charge carries Zn^{2+} and H^+ with the organic NDI electrode. Our fundamental study showed that stepwise electron transfer of the NDI determined the approaching depth of positive charge carriers. The surface-association process occurring for the first discharging process was fast and minimally dependent on either Zn^{2+} or H^+. In contrast, the second discharging region of the NDI underwent solid-state diffusion of the charge carriers through intercalation. The H^+ intercalation became predominant at 1 C rate, and caused the dissolution of the NDI molecules. Numerous H^+ could be supplied through dissociation of water, supported by the precipitation of a zinc hydroxy sulfate. We demonstrated that the suppression of the H^+ intercalation by controlling the discharging depth enhanced the cyclability over 1000 cycles. This study sheds light on the dissolution mechanism of organic electrodes and provides broad implications for developing aqueous batteries with improved stability.

Methods

Synthesis of NDI molecules. Naphthalene diimide (NDI) was synthesized by dissolving 1.25 g of 1,4,5,8-naphthalene-tetracarboxylic dianhydride (NTCDA, Alfa Aesar, 97%) in 62.5 mL of aqueous ammonia solution (Junsei, 28 wt%).[44] The mixture was stirred at room temperature under argon (Ar) condition for 6 h. Afterward, a pale yellow precipitant was filtrated using cellulose membrane (0.1 μm pore size, Millipore) and washed with deionized (DI) water (18.2 MΩ). The NDI powder then dried under 60 °C vacuum overnight.

Preparation of NDI electrodes. To prepare NDI electrodes, NDI, Super P carbon (TIMCAL), and polyvinylidene fluoride (PVdF, HSV 900, Kynar) binder were mixed with 60, 30, and 10 wt%, respectively. NDI powder was firstly ground with Super P carbon, and PVdF binder that was dissolved in N-methyl-2-pyrrolidone (NMP, Sigma Aldrich, 99%) was added. This slurry was subsequently blended using a planetary mixer (THINKY, ARE-310), and cast on a gas diffusion layer (GDL) of carbon paper (BC 39, SGL). After drying under vacuum, the electrode was cut and dried in a vacuum oven at 60 °C overnight. The loading weight of the NDI electrode was typically 1.7—2.8 mg cm^{-2}.

Preparation of Zn–NDI cells. A coin cell was assembled with a metallic Zn foil (Welcos, 99.99%, thickness: 0.05 mm) as the negative electrode, a piece of glass fiber (GF-C, Whatman), and NDI positive electrode in an Ar-filled glovebox (MOTEK, Ar purity 99.999%). A total of 150 μL of the aqueous electrolyte solution, 1 M zinc sulfate ($ZnSO_4$, Sigma Aldrich, 99.9%) was added. These aqueous electrolyte solutions were purged with Ar gas (Daesung, 99.999%) for 5 min before use. For non-aqueous electrolyte solution examinations, the same volume of 1 M $Zn(OTf)_2$ in acetonitrile (Sigma Aldrich, 99.8%) was employed.

Electrochemical examinations. For cyclic voltammogram (CV) tests with different aqueous electrolyte solutions, three-electrode cells were installed. The three-electrode cells were comprised of the NDI electrode as the working electrode (WE), a platinum wire as the counter electrode (CE), and Ag/AgCl as the reference electrode (RE, 0.197 V vs. SHE, EC-Frontier). The aqueous electrolyte solutions were prepared from 1 M HOTf (TCI, 98%), LiOTf (TCI, 98%), NaOTf (Sigma Aldrich, 98%), KOTf (TCI, 98%), $Mg(OTf)_2$ (TCI, 98%), or 1 M zinc trifluoromethanesulfonate ($Zn(OTf)_2$, TCI, 98%) with a volume of ~7.5 mL, and purged with Ar gas at least 5 min prior to examinations. The CV tests were conducted using a single-channel potentiostat (SP-150, Biologic) with mild purging of Ar gas.

Galvanostatic examinations of Zn–NDI cells were conducted using battery cycler (Small cell cycler, PNE solution) after resting at open circuit potential (OCP) for 12 h.

Characterizations. The Zn-NDI cells were disassembled inside of Ar-filled glovebox after electrochemical tests. The NDI electrodes were thoroughly washed with DI water and dried in a glass vacuum oven (B-585, Buchi) at 60 °C for 12 h for X-ray photoelectron spectroscopy (XPS), field emission scanning electron microscopy (FE-SEM), and scanning transmission electron microscopy (STEM) observations. The electrodes for infrared (IR) spectroscopy, solid-state 1H nuclear magnetic resonance (NMR) spectroscopy and X-ray diffraction (XRD) analyses were dried in ambient air overnight. The XPS analysis of the NDI electrode surface was attained from Al Kα X-ray monochromator (K-alpha, Thermo VG Scientific). All samples spectra were calibrated to sp2 hybridized carbon at 248.5 eV in C 1s binding energy region. The intensity of the O 1s spectrum for all galvanostatic tested samples was normalized from the area of N 1s spectrum. The IR spectrum was taken from attenuated total reflection IR (ATR–IR, iS50 built-in diamond ATR module, Thermo Scientific). Solid-state 1H NMR spectroscopy (Agilent 400 MHz, 54 mm NMR, DD2 spectrometer) was measured for tested electrodes to find the water cluster. As the sample preparation, the air-drying NDI electrode was detached from the carbon paper, then ground using a mortar and pestle. The sample spinning was controlled to 30 kHz, and chemical shifts are reported in delta (δ) unit. Powder XRD using Cu Kα radiation and D/tex Ultra 250 detector (SmartLab, RIGAKU) showed a crystalline pattern of NDI and byproduct in the electrodes. In situ XRD measurements were performed using Cu Kα radiation and image plate system (D/MAX-2500, RIGAKU). PDXL Application analysis software and Cambridge crystallographic data center (QEFBUY)[45] were used to identify the crystalline patterns. The FE-SEM, S-4800 (HITACH) and STEM (FEI Tecnai F30 ST, 300 kV, high-angle annular dark-field (HAADF) detector)-incorporated energy dispersive spectrometer (EDS) were used to observe the

morphology of NDI particles and elemental mapping, respectively.

ASSOCIATED CONTENT

Supporting Information: Supporting data analyzed by CV, galvanostatic examinations, XPS, XRD, and SEM (PDF)

AUTHOR INFORMATION

Corresponding Author

* hrbyon@kaist.ac.kr

ACKNOWLEDGMENT

This work is supported by the Samsung Research Funding & Incubation Center of Samsung Electronics under Project Number SRFC-MA1702-05.

REFERENCES

1. Liu, J.; Xu, C.; Chen, Z.; Ni, S.; Shen, Z. X., Progress in aqueous rechargeable batteries. *Green Energy Environ.* **2018,** *3* (1), 20-41.
2. Wang, J.; Yamada, Y.; Sodeyama, K.; Watanabe, E.; Takada, K.; Tateyama, Y.; Yamada, A., Fire-extinguishing organic electrolytes for safe batteries. *Nat. Energy* **2018,** *3* (1), 22-29.
3. Demir-Cakan, R.; Palacin, M. R.; Croguennec, L., Rechargeable aqueous electrolyte batteries: from univalent to multivalent cation chemistry. *J. Mater. Chem. A* **2019,** *7* (36), 20519-20539.
4. Parker, J. F.; Chervin, C. N.; Pala, I. R.; Machler, M.; Burz, M. F.; Long, J. W.; Rolison, D. R., Rechargeable nickel–3D zinc batteries: An energy-dense, safer alternative to lithium-ion. *Science* **2017,** *356* (6336), 415-418.
5. Shin, J.; Lee, J.; Park, Y.; Choi, J. W., Aqueous zinc ion batteries: focus on zinc metal anodes. *Chem. Sci.* **2020,** *11* (8), 2028-2044.
6. Xu, C.; Li, B.; Du, H.; Kang, F., Energetic Zinc Ion Chemistry: The Rechargeable Zinc Ion Battery. *Angew. Chem. Int. Ed.* **2012,** *51* (4), 933-935.
7. Sun, W.; Wang, F.; Hou, S.; Yang, C.; Fan, X.; Ma, Z.; Gao, T.; Han, F.; Hu, R.; Zhu, M.; Wang, C., Zn/MnO2 Battery Chemistry With H+ and Zn2+ Coinsertion. *J. Am. Chem. Soc.* **2017,** *139* (29), 9775-9778.
8. Pan, H.; Shao, Y.; Yan, P.; Cheng, Y.; Han, K. S.; Nie, Z.; Wang, C.; Yang, J.; Li, X.; Bhattacharya, P.; Mueller, K. T.; Liu, J., Reversible aqueous zinc/manganese oxide energy storage from conversion reactions. *Nat. Energy* **2016,** *1* (5), 16039.
9. Wu, X.; Hong, J. J.; Shin, W.; Ma, L.; Liu, T.; Bi, X.; Yuan, Y.; Qi, Y.; Surta, T. W.; Huang, W.; Neuefeind, J.; Wu, T.; Greaney, P. A.; Lu, J.; Ji, X., Diffusion-free Grotthuss topochemistry for high-rate and long-life proton batteries. *Nat. Energy* **2019,** *4* (2), 123-130.
10. Fang, G.; Zhou, J.; Pan, A.; Liang, S., Recent Advances in Aqueous Zinc-Ion Batteries. *ACS Energy Lett.* **2018,** *3* (10), 2480-2501.
11. Shea, J. J.; Luo, C., Organic Electrode Materials for Metal Ion Batteries. *ACS Appl. Mater. Interfaces* **2020,** *12* (5), 5361-5380.
12. Zhao, Q.; Huang, W.; Luo, Z.; Liu, L.; Lu, Y.; Li, Y.; Li, L.; Hu, J.; Ma, H.; Chen, J., High-capacity aqueous zinc batteries using sustainable quinone electrodes. *Sci. Adv.* **2018,** *4* (3), eaao1761.
13. Guo, Z.; Ma, Y.; Dong, X.; Huang, J.; Wang, Y.; Xia, Y., An Environmentally Friendly and Flexible Aqueous Zinc Battery Using an Organic Cathode. *Angew. Chem. Int. Ed.* **2018,** *57* (36), 11737-11741.
14. Nam, K. W.; Kim, H.; Beldjoudi, Y.; Kwon, T.-w.; Kim, D. J.; Stoddart, J. F., Redox-Active Phenanthrenequinone Triangles in Aqueous Rechargeable Zinc Batteries. *J. Am. Chem. Soc.* **2020,** *142* (5), 2541-2548.
15. Nam, K. W.; Kim, H.; Choi, J. H.; Choi, J. W., Crystal water for high performance layered manganese oxide cathodes in aqueous rechargeable zinc batteries. *Energy Environ. Sci.* **2019,** *12* (6), 1999-2009.
16. Yan, M.; He, P.; Chen, Y.; Wang, S.; Wei, Q.; Zhao, K.; Xu, X.; An, Q.; Shuang, Y.; Shao, Y.; Mueller, K. T.; Mai, L.; Liu, J.; Yang, J., Water-Lubricated Intercalation in V2O5·nH2O for High-Capacity and High-Rate Aqueous Rechargeable Zinc Batteries. *Adv. Mater.* **2018,** *30* (1), 1703725.
17. Guin, P. S.; Das, S.; Mandal, P. C., Electrochemical Reduction of Quinones in Different Media: A Review. *Int. J. Electrochem. Sci.* **2011,** *2011*, 816202.
18. Shi, H.-Y.; Ye, Y.-J.; Liu, K.; Song, Y.; Sun, X., A Long-Cycle-Life Self-Doped Polyaniline Cathode for Rechargeable Aqueous Zinc Batteries. *Angew. Chem. Int. Ed.* **2018,** *57* (50), 16359-16363.
19. Tie, Z.; Liu, L.; Deng, S.; Zhao, D.; Niu, Z., Proton Insertion Chemistry of a Zinc–Organic Battery. *Angew. Chem. Int. Ed.* **2020,** *59* (12), 4920-4924.
20. Huang, J.; Wang, Z.; Hou, M.; Dong, X.; Liu, Y.; Wang, Y.; Xia, Y., Polyaniline-intercalated manganese dioxide nanolayers as a high-performance cathode material for an aqueous zinc-ion battery. *Nat. Commun.* **2018,** *9* (1), 2906.
21. Katz, H. E.; Lovinger, A. J.; Johnson, J.; Kloc, C.; Siegrist, T.; Li, W.; Lin, Y. Y.; Dodabalapur, A., A soluble and air-stable organic semiconductor with high electron mobility. *Nature* **2000,** *404* (6777), 478-481.
22. Seydou, M.; Teyssandier, J.; Battaglini, N.; Kenfack, G. T.; Lang, P.; Tielens, F.; Maurel, F.; Diawara, B., Characterization of NTCDI supra-molecular networks on Au(111); combining STM, IR and DFT calculations. *RSC Adv.* **2014,** *4* (49), 25698-25708.
23. Harris, D. C., *Quantitative Chemical Analysis*. W. H. Freeman: 2015.
24. Peover, M. E.; Davies, J. D., The influence of ion-association on the polarography of quinones in dimethylformamide. *J. Electroanal. Chem.* **1963,** *6* (1), 46-53.
25. DeBlase, C. R.; Hernández-Burgos, K.; Rotter, J. M.; Fortman, D. J.; dos S. Abreu, D.; Timm, R. A.; Diógenes, I. C. N.; Kubota, L. T.; Abruña, H. D.; Dichtel, W. R., Cation-Dependent Stabilization of Electrogenerated Naphthalene Diimide Dianions in Porous Polymer Thin Films and Their Application to Electrical Energy Storage. *Angew. Chem. Int. Ed.* **2015,** *54* (45), 13225-13229.
26. Yao, X.; Ke, Y.; Ren, W.; Wang, X.; Xiong, F.; Yang, W.; Qin, M.; Li, Q.; Mai, L., Defect-Rich Soft Carbon Porous Nanosheets for Fast and High-Capacity Sodium-Ion Storage. *Adv. Energy Mater.* **2019,** *9* (6), 1803260.
27. Ding, Y.; Zhang, F.; Xu, J.; Miao, Y.; Yang, Y.; Liu, X.; Xu, B., Synthesis of short-chain passivated carbon quantum dots as the light emitting layer towards electroluminescence. *RSC Adv.* **2017,** *7* (46), 28754-28762.
28. Ferraria, A. M.; Lopes da Silva, J. D.; Botelho do Rego, A. M., XPS studies of directly fluorinated HDPE: problems and solutions. *Polymer* **2003,** *44* (23), 7241-7249.
29. Oh, Y. J.; Yoo, J. J.; Kim, Y. I.; Yoon, J. K.; Yoon, H. N.; Kim, J.-H.; Park, S. B., Oxygen functional groups and electrochemical capacitive behavior of incompletely reduced graphene oxides as a thin-film electrode of supercapacitor. *Electrochim. Acta* **2014,** *116*, 118-128.
30. Pan, D.; Wang, L.; Li, Z.; Geng, B.; Zhang, C.; Zhan, J.; Yin, L.; Wang, L., Synthesis of graphene quantum dot/metal–organic framework nanocomposites as yellow phosphors for white light-emitting diodes. *New J. Chem.* **2018,** *42* (7), 5083-5089.
31. Al-Gaashani, R.; Radiman, S.; Daud, A. R.; Tabet, N.; Al-Douri, Y., XPS and optical studies of different morphologies of ZnO nanostructures prepared by microwave methods. *Ceram. Int.* **2013,** *39* (3), 2283-2292.
32. Stanimirova, T.; Kerestedjian, T.; Kirov, G., Dehydration and rehydration of Zn-hydroxy sulfate minerals with interrupted decorated hydroxide sheets. *Appl. Clay Sci.* **2017,** *135*, 16-26.
33. Zabolotskii, V. I.; Shel'deshov, N. V.; Gnusin, N. P., Dissociation of Water Molecules in Systems with Ion-exchange Membranes. *Russ. Chem. Rev.* **1988,** *57* (8), 801-808.
34. Simons, R., Water splitting in ion exchange membranes. *Electrochim. Acta* **1985,** *30* (3), 275-282.
35. Tanaka, Y., Water dissociation in ion-exchange membrane electrodialysis. *J. Membr. Sci.* **2002,** *203* (1), 227-244.

36. Albery, W. J., Effect of the dissociation of water on electrochemical studies involving hydrogen ions. *Trans. Faraday Soc.* **1966,** *62* (0), 1575-1582.
37. Wang, X.; Bommier, C.; Jian, Z.; Li, Z.; Chandrabose, R. S.; Rodríguez-Pérez, I. A.; Greaney, P. A.; Ji, X., Hydronium-Ion Batteries with Perylenetetracarboxylic Dianhydride Crystals as an Electrode. *Angew. Chem. Int. Ed.* **2017,** *56* (11), 2909-2913.
38. Shi, Y.; Tang, H.; Jiang, S.; Kayser, L. V.; Li, M.; Liu, F.; Ji, F.; Lipomi, D. J.; Ong, S. P.; Chen, Z., Understanding the Electrochemical Properties of Naphthalene Diimide: Implication for Stable and High-Rate Lithium-Ion Battery Electrodes. *Chem. Mater.* **2018,** *30* (10), 3508-3517.
39. Rodríguez-Pérez, I. A.; Yuan, Y.; Bommier, C.; Wang, X.; Ma, L.; Leonard, D. P.; Lerner, M. M.; Carter, R. G.; Wu, T.; Greaney, P. A.; Lu, J.; Ji, X., Mg-Ion Battery Electrode: An Organic Solid's Herringbone Structure Squeezed upon Mg-Ion Insertion. *J. Am. Chem. Soc.* **2017,** *139* (37), 13031-13037.
40. Wilson, H.; Byrne, S.; Bampos, N.; Mullen, K. M., 'Click' functionalised polymer resins: a new approach to the synthesis of surface attached bipyridinium and naphthalene diimide [2]rotaxanes. *Org. Biomol. Chem.* **2013,** *11* (13), 2105-2115.
41. Ando, S.; Harris, R. K.; Holstein, P.; Reinsberg, S. A.; Yamauchi, K., Solid-state 1H-static, 1H-MAS, and 1H→19F/19F→1H CP/MAS NMR study of poly(vinyl fluoride). *Polymer* **2001,** *42* (19), 8137-8151.
42. Bastow, T. J.; Hodge, R. M.; Hill, A. J., 1H and 13C NMR studies of water and heavy water absorption in poly(vinyl alcohol) hydrogels. *J. Membr. Sci.* **1997,** *131* (1), 207-215.
43. Eftekhari, A.; Fang, B., Electrochemical hydrogen storage: Opportunities for fuel storage, batteries, fuel cells, and supercapacitors. *Int. J. Hydrogen Energy* **2017,** *42* (40), 25143-25165.
44. Sotiriou-Leventis, C.; Mao, Z., A facile synthesis of 2,7-diazapyrene. *J. Heterocycl. Chem.* **2000,** *37* (6), 1665-1667.
45. Keeling, D. L.; Oxtoby, N. S.; Wilson, C.; Humphry, M. J.; Champness, N. R.; Beton, P. H., Assembly and Processing of Hydrogen Bond Induced Supramolecular Nanostructures. *Nano Lett.* **2003,** *3* (1), 9-12.

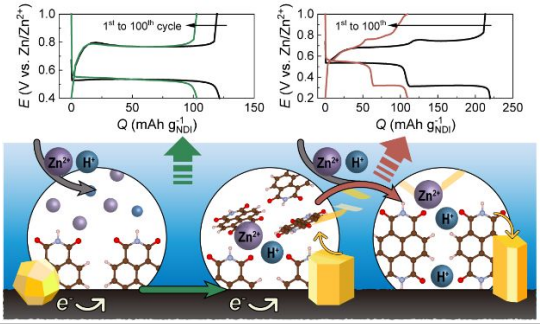
E (V vs. Zn/Zn2+)
1st to 100th cycle
Q (mAh g-1NDI)
1st to 100th
Zn2+
H+
e-